J. Fluid Mech. (2024), *vol*. 986, A2, doi:10.1017/jfm.2024.263

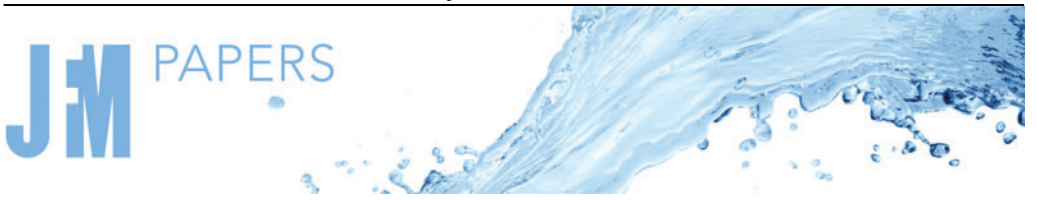

Large-scale patterns set the predictability limit of extreme events in Kolmogorov flow

Alberto Vela-Martín[1],† **and Marc Avila**[1]

[1]Center of Applied Space Technology and Microgravity (ZARM), University of Bremen, 28359 Bremen, Germany

(Received 30 July 2023; revised 4 February 2024; accepted 7 March 2024)

Events of extreme intensity in turbulent flows from atmospheric to industrial scales have a strong social and economic impact, and hence there is a need to develop models and indicators which enable their early prediction. Part of the difficulty here stems from the intrinsic sensitivity to initial conditions of turbulent flows. Despite recent progress in understanding and predicting extreme events, the question of how far in advance they can be ideally predicted (without model error and subject only to uncertainty in the initial conditions) remains open. Here we study the predictability limit of extreme dissipation bursts in the two-dimensional Kolmogorov flow by applying information-theoretic measures to massive statistical ensembles with more than 10^7 direct numerical simulations. We find that extreme events with similar intensity and structure can exhibit disparate predictability due to different causal origins. Specifically, we show that highly predictable extreme events evolve from distinct large-scale circulation patterns. We thus suggest that understanding all the possible routes to the formation of extreme events is necessary to assess their predictability.

Key words: turbulence theory, chaos

1. Introduction

Understanding and predicting extreme events remains an open problem in turbulence research with important theoretical and practical implications. Particularly now, in the context of climate change (Rahmstorf & Coumou 2011; Stott 2016), interest has emerged to develop models and indicators which afford early warnings of extreme events (Travis 2010; Alfieri *et al.* 2012; Vitart & Robertson 2018). These models are usually constructed using variational principles (Farazmand & Sapsis 2017; Blonigan, Farazmand & Sapsis 2019),

† Email address for correspondence: albertovelam@gmail.com

reduced-order modelling (Chen & Majda 2020) or machine learning (Lellep *et al.* 2020; Qi & Majda 2020; Fernex, Noack & Semaan 2021; Lellep *et al.* 2022), and their performance is partly limited by their ability to parse complex dynamics (Kaszás & Haller 2020). A more fundamental limitation stems from the uncertainty in the initial conditions, which is amplified in time by the chaotic dynamics, and imposes a maximum or ideal temporal limit beyond which predictions become impossible (Lorenz 1963).

Predictability is characterised in general by the Lyapunov exponents (Boffetta *et al.* 2002), which measure the rate of separation of trajectories starting from neighbouring initial conditions (Lorenz 1965; Aurell *et al.* 1997; Ziehmann, Smith & Kurths 2000). In particular, the sum of the positive Lyapunov exponents, the Kolmogorov–Sinai entropy, quantifies the rate at which different possible future states emerge from the present state of the system (Boffetta *et al.* 2002). However, the Lyapunov exponents are very sensitive to small-scale dynamics (Aurell *et al.* 1997; Budanur & Kantz 2022) and are only useful to characterise short-time predictability (Palmer 1993). Moreover, their relationship to certain features of the flow, such as extreme events, is not straightforward. Specifically, the predictability of extreme events is not concerned with the number of different possible future states, but with the fraction of them that will be extreme. This information is given by the evolution of probability distributions in the phase space of the system, which is difficult to model due to the high dimension of the chaotic attractor underlying turbulent flows (Epstein 1969; Palmer 2000). In general, it is unclear how far in advance extreme events can be predicted and by how much predictive models can be improved.

In this paper, we investigate the ideal predictability limit of extreme events in a two-dimensional turbulent flow driven by a Kolmogorov (sinusoidal) forcing. We consider the Navier–Stokes equations as a perfect forecasting model, and reproduce the uncertainty of the initial conditions using small random perturbations, a technique known as Monte Carlo forecasting (Epstein 1969). We produce massive ensembles of perturbations to accurately describe the temporal evolution of probability distributions and quantify predictability as the information gained by forecasting under these ideal conditions. We show that the predictability of extreme events fluctuates strongly across the attractor and that it depends on the state from which the extreme event emerges.

2. Forecasting the Kolmogorov flow with massive ensembles

The two-dimensional Kolmogorov flow is spatially extended, deterministic and chaotic, and features some of the complex dynamics of turbulence, in particular, the strong bursting (Kim, Kline & Reynolds 1971; Encinar & Jiménez 2020) and extreme episodes of the dissipation (Hack & Schmidt 2021). It has been widely used as a testbed for reduced-order modelling (Fernex *et al.* 2021), to describe the geometry of the phase space with simple invariant solutions of the equations (Chandler & Kerswell 2013; Lucas & Kerswell 2015; Suri *et al.* 2017; Page, Brenner & Kerswell 2021) and for the prediction of extreme dissipation events (Farazmand & Sapsis 2019; Sapsis 2021). This flow is governed by the two-dimensional Navier–Stokes equations (NSEs) in a doubly periodic square domain of area $L^2 = (2\pi)^2$,

$$\partial_t \omega + \boldsymbol{u} \cdot \boldsymbol{\nabla} \omega = \nu \nabla^2 \omega + f, \tag{2.1}$$

where ν is the kinematic viscosity, $\omega = (\boldsymbol{\nabla} \times \boldsymbol{u})_z$ is the vorticity in z (the direction normal to the x–y plane) and $\boldsymbol{u}$ is the velocity vector, which satisfies the incompressibility condition, $\boldsymbol{\nabla} \cdot \boldsymbol{u} = 0$, and is obtained from ω using a stream function. The forcing of the flow acts on the velocity field as $\boldsymbol{f}_u = \{f_0(L/2\pi)\cos(2\pi n_f y/L), 0\}$, where f_0 is the forcing

magnitude and $n_f = 4$ its wavenumber. In the vorticity equation (2.1), the forcing reads

$$f = f_0 n_f \sin(2\pi n_f y/L). \tag{2.2}$$

The flow is characterised by a Reynolds number,

$$Re = f_0^{1/2}(L/2\pi)^2/\nu, \tag{2.3}$$

as defined by Chandler & Kerswell (2013) and Farazmand & Sapsis (2017). In this work, we set $Re = 100$. The vorticity is normalised with $f_0^{1/2}$ and the time with the Lyapunov time, $T_\lambda = \lambda^{-1}$, where λ is the leading Lyapunov exponent, which is calculated following a rescaling method over a long trajectory (Wolf *et al.* 1985). For comparison, the time scale of the forcing is $T_f = 1/f_0{}^{1/2} = 0.28T_\lambda$ and the eddy turnover time is $T_{eto} = (\nu/\bar{\varepsilon})^{1/2} = 1.92T_\lambda$, where the overline denotes temporal average and ε is the spatially averaged energy dissipation. Another important time scale is the delay between energy injection due to the forcing and the dissipation, $T_I = 0.66T_\lambda$, which we obtained from their temporal cross-correlation.

The flow is integrated using a pseudo-spectral method with a Fourier basis of $N/2$ modes in each direction, where $N = 128$ is the number of points in physical space. This is similar to the resolution used by Lucas & Kerswell (2015). The nonlinear terms are fully dealiased using a 2/3 rule, and a third-order low-storage Runge–Kutta method is used for time marching. The simulations are carried out using a GPU code based on the spectral solver described by Cardesa, Vela-Martín & Jiménez (2017), which enables a massive exploration of phase space at a moderate cost.

We aim to determine the predictability of the instantaneous space-averaged enstrophy,

$$\Omega = \langle \omega^2 \rangle, \tag{2.4}$$

where the brackets denote the spatial average over the computational domain. Note that $\Omega = \varepsilon/\nu$, so we interchangeably use dissipation and enstrophy throughout. We use the Navier–Stokes equations as a perfect forecasting model so that uncertainty is only due to the initial conditions. First, we sample the chaotic attractor with a set of $N_i = 8192$ independent states ω_i, hereafter termed base flows. These base flows represent possible states of the system from which an extreme enstrophy event may eventually arise, as exemplified for two cases in figure 1. This figure shows two events of magnitude $\Omega \approx 9$, which correspond to the upper 1 % of the enstrophy probability distribution in the attractor. The average waiting time between events of this magnitude is more than $90T_\lambda$. Despite the marked differences between the initial circulation patterns in the first and second rows, at peak enstrophy, the flow patterns are remarkably similar in topology and intensity.

We assess the predictability of the $N_i = 8192$ base flows by performing a Monte Carlo ensemble forecast (Leith 1974; Leutbecher & Palmer 2008), in which the uncertainty in the initial state of the system is modelled by small random perturbations. Around each base flow $\omega_i(\boldsymbol{x}, t_0)$, we produce $N_p = 8192$ perturbed flows,

$$\omega_{i,p}(\boldsymbol{x}, t_0) = \omega_i(\boldsymbol{x}, t_0) + \phi(\boldsymbol{x}), \tag{2.5}$$

with a different realisation of the random perturbation field, $\phi(\boldsymbol{x})$, which is Gaussian noise with a white spectrum and variance $\sigma^2 = 0.01 f_0$. In the perturbed fields, $\omega_{i,p}$, the first subscript refers to the base flow and the second subscript to the perturbation. The small magnitude of the initial perturbations ensures that they first evolve according to the linearised dynamics and that they have time to align with the most unstable local directions before triggering nonlinear effects. Thus, the results are independent of the

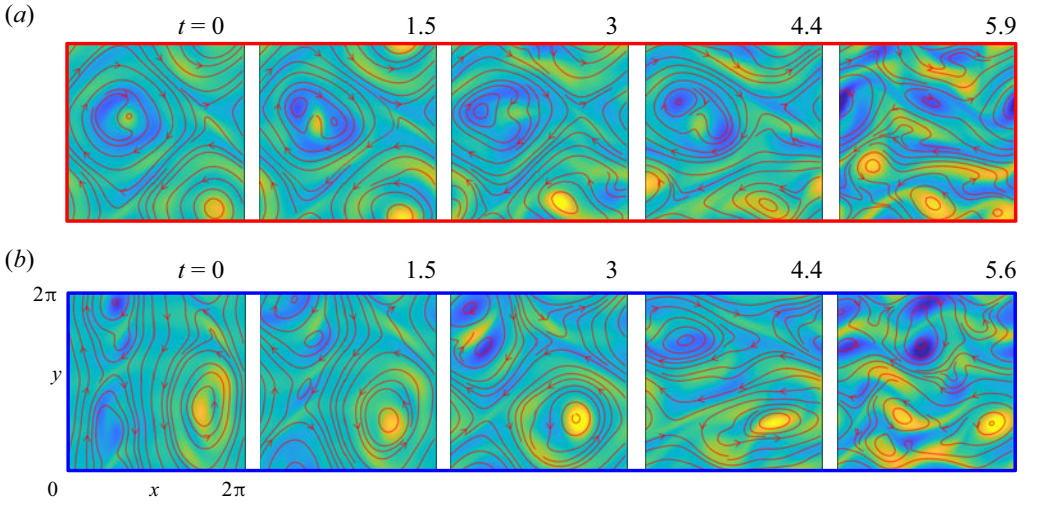

Figure 1. Visualisations of two independent realisations of the Kolmogorov flow (*a*,*b*) before and during an enstrophy burst of magnitude $\Omega > 9$; the corresponding time series of $\Omega(t)$ are shown in figure 2(*a*,*d*). Time goes from left to right, $t = 0$, 1.5, 3, 4.4 and t_e, where $t_e = 5.9$ and $t_e = 5.6$ is the time of the extreme event in the runs in panels (*a*) and (*b*), respectively. The colour map shows the vorticity, ω, from -8 (dark blue) to 8 (yellow), and the red lines are streamlines of the instantaneous velocity field. Initially, the flow is organised in large-scale swirls, sometimes with the presence of vertical velocity jets (bottom-left panel), whereas during the burst, the vorticity is predominantly aligned horizontally, parallel to the forcing driving the flow.

structure of the random perturbation. We have verified this by perturbing the velocity field (instead of the vorticity field) with the same magnitude of the random perturbations. The corresponding analysis is described in Appendix A. Predictability depends naturally on the initial uncertainty, i.e. on the variance of the noise, σ^2, but given its magnitude, this dependence is weak and only relevant for the initial stage of perturbation growth. This stage, which in our ensembles corresponds to a time of the order of T_λ, increases only logarithmically with decreasing σ^2 due to the exponential growth of perturbations with time (see Appendix A).

In summary, we produced $N_i = 8192$ ensembles with $N_p = 8192$ members, which were integrated in time, together with their base states, for 20 Lyapunov times. To study the predictability of the enstrophy, we stored its temporal evolution, $\Omega_{i,p}(t)$, in the $N_i N_p = 2^{26} = 67\,108\,864$ runs. The probability density function (p.d.f.) of $\Omega_{i,p}(t)$ of each ensemble i, denoted by $P_i(t)$, fully describes the possible values of the enstrophy and their likelihood at a future time t. In the next section, we show how $P_i(t)$ can be used to unambiguously quantify the predictability of Ω and, in particular, of its extreme events.

3. Quantifying the predictability of extreme events with information-theoretic measures

In figure 2(*a*), we show the temporal evolution of $\Omega_i(t)$ in the base flow displayed in figure 1(*a*), and the values of $\Omega_{i,p}$ contained between the first and last deciles of $P_i(t)$, represented as a shaded area. Initially, the values of the dissipation in the ensemble remain close to the base flow. Subsequently, the range of possible values of $\Omega_{i,p}$ starts increasing noticeably in a time of the order of the Lyapunov time, indicating that the ensemble is being spread across the attractor. In figure 2(*b*), we show snapshots of $P_i(t)$ at selected times. Initially, P_i has a small spread, but this increases with time. At the time of the

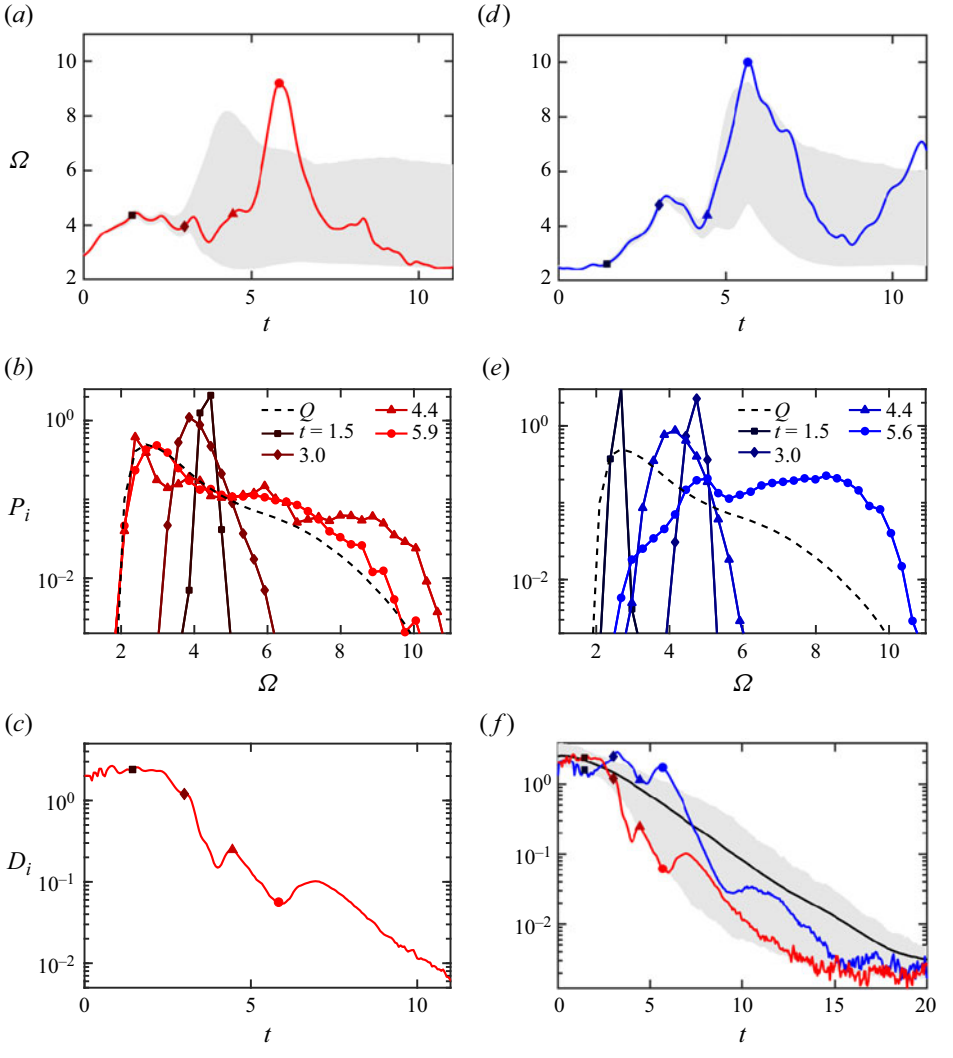

Figure 2. (*a*) Temporal evolution of the enstrophy $\Omega_i(t)$ (red solid line) in the base trajectory visualised in figure 1(*a*). The shaded area spans from the first to the last decile of $\Omega_{i,p}(t)$ in the corresponding ensemble. The markers denote the instants in time shown in figure 1(*a*). (*b*) Forecast probability distribution $P_i(t)$ at the time instants indicated in the legend and marked with points in figure 1(*a*). The climatological distribution Q is shown as a dashed line. (*c*) Temporal evolution of the Kullback–Leibler divergence, $D_i(t)$, for the base trajectory in figure 1(*a*). The points are as in figure 1(*a*). (*d*,*e*) As in panels (*a–c*), but for the predictable base trajectory in figure 1(*b*). In panel (*f*), the shaded are spans from the first to the last decile of the KLD in all the ensembles.

extreme event in the base trajectory, $t_e = 5.9$, the forecast distribution $P_i(t)$ is very similar to the (stationary) probability distribution of Ω in the attractor, Q, which is known as the climatological distribution (DelSole 2004). Hence, with the level of uncertainty in the initial conditions (set by $\phi(\boldsymbol{x})$ in (2.5)), forecasts obtained by solving the NSE are hardly more accurate than the null forecast, i.e. with the assumption that the initial condition was taken randomly from anywhere in the attractor. This means that, given the initial uncertainty, this extreme event is fundamentally unpredictable regardless of the forecasting model in a time horizon of $6T_\lambda$.

Predictability may be quantified with information-theoretic measures of how different $P_i(t)$ is from the climatological probability distribution (Kleeman & Majda 2005; DelSole & Tippett 2007). We use the Kullback–Leibler divergence (KLD)

$$D_i(P_i(t) \mid Q) = \sum \tilde{P}_i(t) \log \frac{\tilde{P}_i(t)}{\tilde{Q}}, \tag{3.1}$$

where the tilde indicates that the probability distributions have been discretised in 40 intervals of equal width in the range [1.5, 13.5], which contain all the samples in the database. The summation is taken over these probability intervals. We have checked that reducing the number of members in the ensemble by a half produces only small variations of D_i. The KLD is always positive unless $P_i(t) = Q$, when it is zero (MacKay 2003). The more that $P_i(t)$ differs from Q, the larger D_i and the more informative the ensemble forecast. In other words, D_i is a measure of the amount of information we gain by forecasting with massive ensembles of NSE simulations with respect to taking the climatological distribution as the forecasting model (null forecast).

The temporal evolution of D_i for the base trajectory in figure 1(*a*) is shown in figure 2(*c*). It fluctuates, as has been observed previously for other information-theoretic measures in low-dimensional systems (Latora & Baranger 1999), but decreases overall with time. At the time of the extreme event in the base trajectory, the KLD has decreased by more than one order of magnitude with respect to its initial value, signalling the lack of information in the forecast distribution and the unpredictability of the extreme event, given the initial uncertainty.

We now examine the predictability of the extreme event displayed in figure 1(*b*). As shown in figure 2(*d*), this extreme event occurs at $t_e \approx 5.6$ and has a magnitude similar to the event examined above. The evolution of the probability distribution of the ensemble, $P_i(t)$, is shown in figure 2(*e*). For this base flow, the probability distribution at t_e is highly skewed towards large values, indicating that this extreme event is largely predictable. In figure 2(*f*), we show the temporal evolution of D_i for the predictable (blue) and unpredictable (red) extreme events. There is a difference of an order of magnitude between their D_i at the time of the extreme event. This is particularly remarkable given that the temporal evolution of Ω, and the flow patterns near the maximum enstrophy, are qualitatively similar. In figure 2(*f*), we have also plotted the evolution of the average (solid black line) and the first and last deciles (shaded area) of D_i in the 8192 base flows. Again, there is a difference of more than one order of magnitude between the first and last deciles, indicating that the strong fluctuations of predictability between the two trajectories of figure 1 are a general, intrinsic feature of the system.

The strong fluctuations in predictability are confirmed using another indicator: the ratio of successful predictions (RSPs) (Farazmand & Sapsis 2017). For each base trajectory i, we define an extreme event happening at time t_e as a local maximum of Ω_i in which $\Omega_i > \alpha$, where α is a threshold. Now, we consider each ensemble member p as an individual forecast and tag this forecast as successful (true positive) if it gives $\Omega_{i,p} > \alpha$ at the time of the extreme event in the base trajectory, t_e. However, we tag this forecast as unsuccessful (false negative) if it gives $\Omega_{i,p} < \alpha$ at t_e. In each ensemble, we calculate the number of true positives, $N_{true\ pos.}$ and false negatives $N_{false\ neg.}$, and define the RSP as

$$RSP = \frac{N_{true\ pos.}}{N_{true\ pos.} + N_{false\ neg.}}, \tag{3.2}$$

which depends on the time of the extreme event in the base trajectory, t_e, and on the threshold α. Since the number of members in the ensemble is $N_p = N_{true\ pos.} + N_{false\ neg.}$,

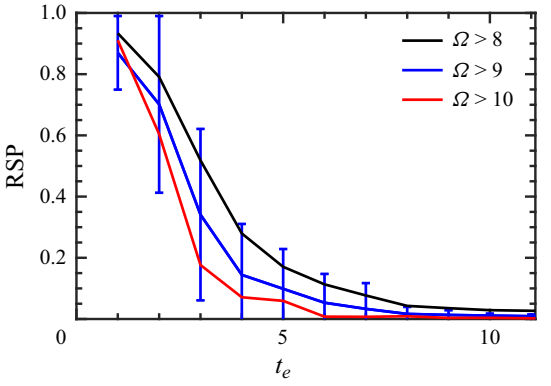

Figure 3. Average RSP as a function of the time of extreme events, t_e, for different thresholds: $\Omega > 8$ (black line); $\Omega > 9$ (blue line); $\Omega > 10$ (red line). The average is calculated in time intervals centred at multiples of T_λ and width T_λ. The bars in the blue line correspond to the mean plus-minus the standard deviation of the RSP in each interval (except when it is negative). For ease of visualisation, bars are only plotted for $\Omega > 9$, but are comparable for the other two cases.

the RSP is defined as the probability that $\Omega_{i,p} > \alpha$ at t_e. In brief, the RSP quantifies the probability of making a successful forecast considering the initial uncertainty and taking the base trajectory as the true trajectory. Here the idea of successful prediction is considered with respect to an ideal forecasting model, i.e. the NSE, which is free of model uncertainty.

In figure 3, we show the RSP averaged over temporal intervals of width T_λ, centred at integer times, for different thresholds. The RSP decreases on average with time and with the intensity of the extreme event. The standard deviation of the RSP in the intervals, shown as bars in the figure, is of the order of the average, corroborating the fluctuations of predictability measured by the KLD. In particular, for the event in figure 1(*b*), the probability that $\Omega_{p,i} > 8.0$ at t_e is close to 50 % ($RSP = 0.5$), indicating that this event is largely predictable. By contrast, for the unpredictable extreme event in figure 1(*a*), this probability is less than 3 % ($RSP = 0.03$).

4. Large-scale circulation patterns set the predictability limit of extreme events

In the following, we perform a conditional statistical analysis to determine the differences between predictable and unpredictable extreme events. From the $N_i = 8192$ base flows, we select those that exhibit a local maximum of the enstrophy in the time interval $3 < t_e < 17$ in which $\Omega_i(t_e) > 8$, where t_e is the time of the maximum. We find that a total of 1040 trajectories satisfy these criteria. The average enstrophy of this group of base trajectories, centred about t_e, is shown as a black line in figure 4(*a*). It remains close to the average in the attractor (shown as a horizontal dotted line) up to approximately $t - t_e \sim -3$, when it shoots up monotonically towards the extreme event.

Within this group, we define two subgroups with high and low predictability, corresponding to the base trajectories above the last and below the first decile of $D_i(t_e)$, respectively. These two groups comprise 167 extreme events which are predictable (above the last decile of D_i) and 174 which are unpredictable (below the first decile of D_i). Before the extreme event, the average enstrophy of the base trajectories in the group with unpredictable extreme events (shown as a red line) is 15 % above the unconditional average. By contrast, the extreme events in the predictable group (blue

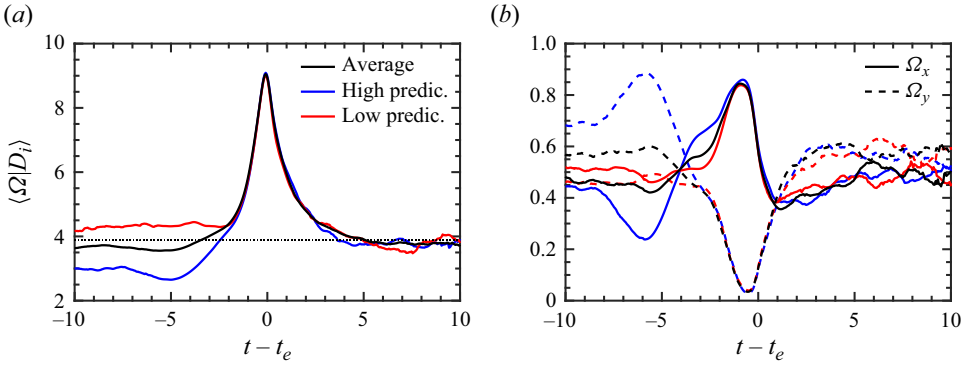

Figure 4. (*a*) Conditional average dissipation. The black line shows the average of Ω_i over all base trajectories featuring an extreme event (with $\Omega_i(t_e) > 8$, for $3 < t_e < 17$). The red and blue lines show the average conditional to low and high predictability, respectively. The corresponding trajectories have a $D_i(t)$ below and above the first and last deciles. The dotted line shows the long-term average of Ω over the attractor. (*b*) Conditional average of the enstrophy contained in the horizontal and vertical large-scale modes, Ω_x and Ω_y. Colours as in panel (*a*). In panels (*a*) and (*b*), we have moved the time origin to the time of the extreme event.

line) are preceded by a quiescent phase with approximately 25 % lower-than-average enstrophy. Approximately two Lyapunov times before and after the extreme event, the evolution of the enstrophy in the predictable and unpredictable events is indistinguishable from the unconditional average. This suggests that the structure of extreme events in the Kolmogorov flow is similar regardless of their predictability, in line with the similarity of the flow patterns in the rightmost panels of figure 1(*a*,*b*).

We now examine the circulation patterns preceding predictable extreme events to search for early signatures of predictability. For this analysis, we Fourier-transform the vorticity field, $\hat{\omega}(\boldsymbol{k}, t) = \mathcal{F}(\omega(\boldsymbol{x}, t))$, where $\boldsymbol{k} = (k_x, k_y)$ is the wavenumber vector. Then we calculate the magnitude of the modes with wavenumbers $\boldsymbol{k}_{||} = (0, \pm 1)$, which represent the vorticity generated by two infinite sinusoidal jets of width $L/2$ in the direction parallel to the forcing (x), and $\boldsymbol{k}_{\perp} = (\pm 1, 0)$, which represent the vorticity generated by the same configuration but in the direction perpendicular to the forcing (y). The enstrophy of these modes is defined as

$$\Omega_x(t) = \sum_{\boldsymbol{k}_{||}} \hat{\omega}(\boldsymbol{k}_{||}, t)\hat{\omega}^*(\boldsymbol{k}_{||}, t) \tag{4.1}$$

and

$$\Omega_y(t) = \sum_{\boldsymbol{k}_{\perp}} \hat{\omega}(\boldsymbol{k}_{\perp}, t)\hat{\omega}^*(\boldsymbol{k}_{\perp}, t), \tag{4.2}$$

where the asterisk represents the complex conjugate, and the summation is taken over pairs of modes.

The predictable extreme event shown in figure 1(*b*) originates from a base flow that exhibits two conspicuous vertical jets of opposite sign separated by elongated vortices of opposite circulation (first panel). For this specific base flow, the contribution to the enstrophy arising from the large-scale vertical flow, Ω_y, clearly exceeds the horizontal contribution, Ω_x. Specifically, at $t = 0$, which corresponds to 5.6 Lyapunov times before the extreme event ($t - t_e = -5.6$), $\Omega_y = 12.3\Omega_x$, whereas for the base flow shown in figure 1(*a*), the circulation pattern displays two coherent vortices without a strong orientation and $\Omega_y = 1.06\Omega_x$ at $t = 0$ ($t - t_e = -5.9$).

In view of this marked difference, we compute conditional averages of Ω_x and Ω_y in the groups of highly predictable and highly unpredictable extreme events, as defined in the previous section. The conditional averages shown in figure 4(*b*) confirm that highly predictable extreme events are preceded at $t - t_e \approx -6$ by a large-scale jet that is predominantly aligned perpendicular to the forcing (in this group, $\Omega_y = 3.7\Omega_x$ on average at this time). However, extreme events with low predictability are preceded by $\Omega_y \approx \Omega_x$, which is slightly lower than the unconditional average ($\Omega_y = 1.3\Omega_x$, not shown). Regardless of the predictability, slightly before the burst ($t - t_e \approx -1$), the large-scale flow is mostly oriented in the direction parallel to the forcing, and hence the contribution of the horizontal jet mode dominates, $\Omega_x > 20\Omega_y$. The maximum of the energy injection happens approximately $0.5T_\lambda$ after this point ($t - t_e \approx -0.5T\lambda$) due to the energy transfer from the jet-mode represented by Ω_y to the forcing mode through a third mode that completes a triad interaction (Farazmand & Sapsis 2019). This time is comparable to the prediction time obtained with a variational method (Farazmand & Sapsis 2017).

Finally, we point out that the base flow generating the predictable enstrophy burst shown in figure 1(*b*) resembles an unstable equilibrium solution (Chandler & Kerswell 2013) that dominates the quiescent, low-enstrophy dynamics of the Kolmogorov flow. Interestingly, experiments of a similar Kolmogorov flow, but at a much lower Reynolds number, demonstrated that the temporal evolution of the flow may be forecasted when certain unstable equilibrium solutions are shadowed by the dynamics (Suri *et al.* 2017). Such a connection between simple solutions of the governing equations and extreme events deserves further investigation and may be a stepping stone to construct predictive algorithms (Cvitanović 1991; Yalnız, Hof & Budanur 2021; Cenedese *et al.* 2022).

5. Conclusion

We determined the predictability of extreme events in a turbulent flow by studying the evolution of massive Monte Carlo ensembles (Leith 1974) to which we applied information-theoretic measures (DelSole 2004). For some specific large-scale configurations, it is theoretically possible to produce informative predictions of extreme events several Lyapunov times in advance. This is an order of magnitude longer than the prediction times computed for the same Kolmogorov flow with variational principles (Farazmand & Sapsis 2017) or machine-learning methods (Fernex *et al.* 2021). Given the small magnitude of the uncertainty we used in the ensemble forecasting, this means that for these specific large-scale configurations, predictive models still have room for improvement. By contrast, extreme events of similar structure and magnitude that emerge from other patterns are impossible to forecast in the same horizon regardless of the model, because even massive ensembles of NSE solutions produce the null forecast.

Our approach considers the full complexity of the chaotic attractor, meaning that for the same initial uncertainty, the forecast distributions computed here cannot be improved by any method. This was possible due to the simplicity of the Kolmogorov flow, for which the Navier–Stokes equations could be solved accurately millions of times at a moderate computational cost, obviating the need for approximate indicators of predictability (Aurell *et al.* 1997; Ziehmann *et al.* 2000). With the available computing power, this approach can be applied to simple atmospheric circulation models to study the predictability of extreme events, for instance, those that emerge from Rossby waves (Boers *et al.* 2019; Kornhuber *et al.* 2020). Other examples of extreme events in turbulence to which massive ensemble forecasting could be applied are the relaminarisation of transitional flows (Hof *et al.* 2006), bursting in near-wall turbulence (Encinar & Jiménez 2020), cavitation inception in small-scale turbulence (Bappy *et al.* 2022) or inertial drop breakup

(Vela-Martín & Avila 2022). The control of turbulent flows in general, and of extreme events in particular, is another application in which massive ensemble forecasting could be used to optimally select target states, or to devise efficient actuators under measurement and actuation uncertainty (Bewley, Moin & Temam 2001). Beyond this applied scope, ensemble forecasting could also constitute an important tool to characterise fundamental aspects of turbulence, such as complexity (Grassberger 1986) or causal relations in a temporal frame (Lozano-Durán, Bae & Encinar 2020).

In conclusion, similar extreme events can be caused by different processes and hence exhibit disparate predictability. Extended to atmospheric sciences, our results would imply that seemingly similar extreme weather events may originate from different circulation patterns, which determine their predictability limit. Hence, constructing and assessing the skill of predictive models, particularly those based on data-driven approaches, requires an exhaustive characterisation of all possible formation routes to extreme events. This is an extremely challenging problem which demands further developments in turbulence modelling, computational methods for fluid dynamics and general circulation models, and rare-event sampling algorithms (Mohamad & Sapsis 2018; Gomé, Tuckerman & Barkley 2022; Rolland 2022).

Funding. The authors gratefully acknowledge support from the Deutsche Forschungsgemeinschaft within the Priority Programme Turbulent Superstructures SPP 1881 under grant no. 316065285 and computing resources provided by the Erlangen National High Performance Computing Center (NHR@FAU) of the Friedrich-Alexander-Universität Erlangen-Nürnberg (FAU) under an early-access NHR project.

Declaration of interests. The authors report no conflict of interest.

Data availability. The numerical data that support the findings of this study are available in Pangaea (https://doi.pangaea.de/10.1594/PANGAEA.967265).

Author ORCIDs.
Alberto Vela-Martín https://orcid.org/0000-0003-4561-8683;
Marc Avila https://orcid.org/0000-0001-5988-1090.

Appendix A. Dependence of the ensemble forecasts on the initial perturbation

In this appendix, we show the effect of changing the structure and magnitude of the perturbations used to generate the initial conditions of the ensembles. In the first case, modifying the structure of the perturbation does not change the evolution of the probability distributions of $\Omega_{i,p}$. To show this, we compare the ensembles generated by perturbing the vorticity field with ensembles produced by perturbing the velocity field using the same noise,

$$u_{i,p}(\boldsymbol{x}, t_0) = u_i(\boldsymbol{x}, t_0) + \phi(\boldsymbol{x}), \tag{A1}$$

$$v_{i,p}(\boldsymbol{x}, t_0) = v_i(\boldsymbol{x}, t_0) + \phi(\boldsymbol{x}), \tag{A2}$$

where u and v are the components of the velocity vector field, $\boldsymbol{u} = \{u, v\}$. After calculating $\omega_{i,p}$ from $\boldsymbol{u}_{i,p}$, the variance of the perturbation in the vorticity field is scaled to $\sigma^2 = 0.01 f_0$. Although this perturbation has a very different structure compared with (2.5), it does not modify the evolution of $\Omega_{p,i}$. To test this, we computed the KLD between $P_i(t)$ (obtained by perturbing the vorticity field, as in the paper) and $P_i^*(t)$ (calculated with the ensembles perturbed on the velocity field) in 16 base trajectories, including two of the base trajectories selected for the conditional analysis of predictable and unpredictable extreme events. The difference between the two distributions is very small, $D_i(P_i(t) \,|\, P_i^*(t)) \approx D_i(P_i^*(t) \,|\, P_i(t)) \sim 10^{-3}$. This similarity is illustrated in figure 5(*a–d*), in which P_i and

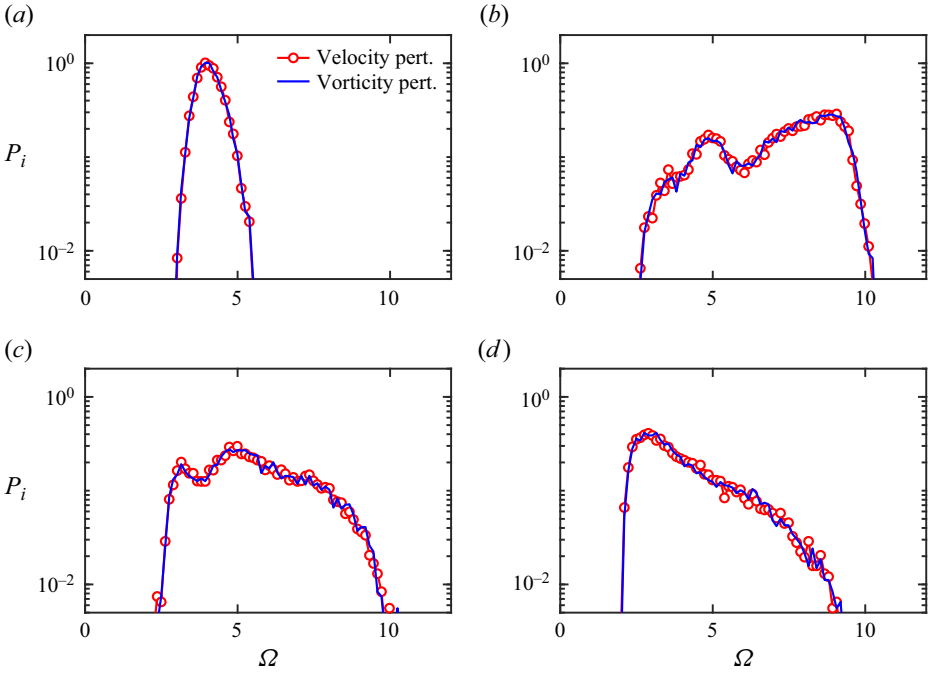

Figure 5. Forecast probability distribution of a single base flow, $P_i(t)$, for ensembles with perturbations in the vorticity and velocity fields. Time corresponds to $t =$: (*a*) 4.4; (*b*) 5.4; (*c*) 6.5; (*d*) 8.8.

P_i^* generated from a single base flow are plotted together at different times. The collapse is very good and the slight differences are due to the finite number of samples.

The magnitude of the perturbation naturally affects the predictability horizon but in a weak way. We produced ensembles of initial perturbations with $\sigma^2 = 0.001 f_0$ and compared it with the ensembles analysed in the paper ($\sigma^2 = 0.01 f_0$). To characterise error growth, we consider the space-averaged enstrophy of the difference between the perturbed trajectories and the base flows, and average it over base flows and perturbed trajectories,

$$\Delta\Omega = \frac{1}{N_i N_p} \sum_{i,p} \langle (\omega_{i,p} - \omega_i)^2 \rangle, \tag{A3}$$

where the averages are taken over $N_i = 128$ independent base flows and $N_p = 128$ perturbations. In figure 6, we show the logarithm of $\Delta\Omega$ as a function of time for the two values of σ^2. Initially, there is a sharp decay of $\Delta\Omega$ due to viscosity, which damps the high frequencies of the perturbations very fast. This regime lasts approximately until $t = 0.25$. After this, the range of exponential growth begins, which is visible as a straight line with slope 1 (due to the normalisation of time with the Lyapunov exponent). The saturation of the exponential growth starts at $t \approx 1.5$ for $\sigma^2 = 0.01 f_0$ and at $t = 4$ for $\sigma^2 = 0.001 f_0$, and corresponds to the beginning of the nonlinear predictability regime. As expected, reducing the initial uncertainty increases predictability. This, however, only affects the initial exponential regime. Considering that $\Delta\Omega \propto \exp t$ in Lyapunov-time units, the effect of reducing the perturbation by 10 is equivalent to a temporal offset of $\log 10 \approx 2.3$. This is corroborated by the good collapse in figure 6 between the evolution of the perturbations for $\sigma^2 = 0.01 f_0$ and for $\sigma^2 = 0.001 f_0$ when the latter is time-shifted towards the past by 2.3

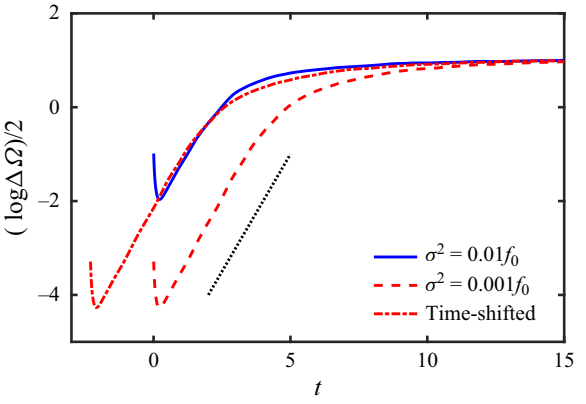

Figure 6. Temporal evolution of the logarithm of $\Delta\Omega$ for different magnitudes of the initial perturbations, $\sigma^2 = 0.01 f_0$ and $\sigma^2 = 0.001 f_0$. The dash-dotted curve corresponds to the data for $\sigma^2 = 0.001 f_0$, but shifted towards the past by $\log 10 = 2.3$ Lyapunov times. The dotted line has slope 1. The $1/2$ factor is used for consistency with the definition of Lyapunov exponent.

Lyapunov times. Thus, due to the small magnitude of σ^2, further reducing the uncertainty only adds to the short-time predictability range.

References

Alfieri, L., Salamon, P., Pappenberger, F., Wetterhall, F. & Thielen, J. 2012 Operational early warning systems for water-related hazards in Europe. *Environ. Sci. Policy* **21**, 35–49.

Aurell, E., Boffetta, G., Crisanti, A., Paladin, G. & Vulpiani, A. 1997 Predictability in the large: an extension of the concept of Lyapunov exponent. *J. Phys.* A **30** (1), 1.

Bappy, M.H., Carrica, P.M., Li, J., Martin, J.E., Vela-Martín, A., Freire, L.S. & Buscaglia, G.C. 2022 A sub-grid scale cavitation inception model. *Phys. Fluids* **34** (3), 033308.

Bewley, T.R., Moin, P. & Temam, R. 2001 Dns-based predictive control of turbulence: an optimal benchmark for feedback algorithms. *J. Fluid Mech.* **447**, 179–225.

Blonigan, P.J., Farazmand, M. & Sapsis, T.P. 2019 Are extreme dissipation events predictable in turbulent fluid flows? *Phys. Rev. Fluids* **4** (4), 044606.

Boers, N., Goswami, B., Rheinwalt, A., Bookhagen, B., Hoskins, B. & Kurths, J. 2019 Complex networks reveal global pattern of extreme-rainfall teleconnections. *Nature* **566** (7744), 373–377.

Boffetta, G., Cencini, M., Falcioni, M. & Vulpiani, A. 2002 Predictability: a way to characterize complexity. *Phys. Rep.* **356** (6), 367–474.

Budanur, N.B. & Kantz, H. 2022 Scale-dependent error growth in Navier–Stokes simulations. *Phys. Rev.* E **106** (4), 045102.

Cardesa, J.I., Vela-Martín, A. & Jiménez, J. 2017 The turbulent cascade in five dimensions. *Science* **357** (6353), 782–784.

Cenedese, M., Axas, J., Bäuerlein, B., Avila, K. & Haller, G. 2022 Data-driven modeling and prediction of non-linearizable dynamics via spectral submanifolds. *Nat. Commun.* **13** (1), 872.

Chandler, G.J. & Kerswell, R.R. 2013 Invariant recurrent solutions embedded in a turbulent two-dimensional Kolmogorov flow. *J. Fluid Mech.* **722**, 554–595.

Chen, N. & Majda, A.J. 2020 Predicting observed and hidden extreme events in complex nonlinear dynamical systems with partial observations and short training time series. *Chaos* **30** (3), 033101.

Cvitanović, P. 1991 Periodic orbits as the skeleton of classical and quantum chaos. *Physica* D **51** (1–3), 138–151.

DelSole, T. 2004 Predictability and information theory. Part 1. Measures of predictability. *J. Atmos. Sci.* **61** (20), 2425–2440.

DelSole, T. & Tippett, M.K. 2007 Predictability: recent insights from information theory. *Rev. Geophys.* **45** (4).

Encinar, M.P. & Jiménez, J. 2020 Momentum transfer by linearised eddies in turbulent channel flows. *J. Fluid Mech.* **895**, A23.

EPSTEIN, E.S. 1969 Stochastic dynamic prediction. *Tellus* **21** (6), 739–759.
FARAZMAND, M. & SAPSIS, T.P. 2017 A variational approach to probing extreme events in turbulent dynamical systems. *Sci. Adv.* **3** (9), e1701533.
FARAZMAND, M. & SAPSIS, T.P. 2019 Extreme events: mechanisms and prediction. *Appl. Mech. Rev.* **71** (5), 050801.
FERNEX, D., NOACK, B.R. & SEMAAN, R. 2021 Cluster-based network modeling–from snapshots to complex dynamical systems. *Sci. Adv.* **7** (25), eabf5006.
GOMÉ, S., TUCKERMAN, L.S. & BARKLEY, D. 2022 Extreme events in transitional turbulence. *Phil. Trans. R. Soc.* A **380** (2226), 20210036.
GRASSBERGER, P. 1986 Toward a quantitative theory of self-generated complexity. *Intl J. Theor. Phys.* **25**, 907–938.
HACK, M.J.P. & SCHMIDT, O.T. 2021 Extreme events in wall turbulence. *J. Fluid Mech.* **907**, A9.
HOF, B., WESTERWEEL, J., SCHNEIDER, T.M. & ECKHARDT, B. 2006 Finite lifetime of turbulence in shear flows. *Nature* **443** (7107), 59–62.
KASZÁS, B. & HALLER, G. 2020 Universal upper estimate for prediction errors under moderate model uncertainty. *Chaos* **30** (11), 113144.
KIM, H.T., KLINE, S.J. & REYNOLDS, W.C. 1971 The production of turbulence near a smooth wall in a turbulent boundary layer. *J. Fluid Mech.* **50** (1), 133–160.
KLEEMAN, R. & MAJDA, A. 2005 Predictability in a model of geophysical turbulence. *J. Atmos. Sci.* **62** (8), 2864–2879.
KORNHUBER, K., COUMOU, D., VOGEL, E., LESK, C., DONGES, J.F., LEHMANN, J. & HORTON, R.M. 2020 Amplified Rossby waves enhance risk of concurrent heatwaves in major breadbasket regions. *Nat. Clim. Change* **10** (1), 48–53.
LATORA, V. & BARANGER, M. 1999 Kolmogorov-Sinai entropy rate versus physical entropy. *Phys. Rev. Lett.* **82** (3), 520.
LEITH, C.E. 1974 Theoretical skill of Monte Carlo forecasts. *Mon. Weath. Rev.* **102** (6), 409–418.
LELLEP, M., PREXL, J., ECKHARDT, B. & LINKMANN, M. 2022 Interpreted machine learning in fluid dynamics: explaining relaminarisation events in wall-bounded shear flows. *J. Fluid Mech.* **942**, A2.
LELLEP, M., PREXL, J., LINKMANN, M. & ECKHARDT, B. 2020 Using machine learning to predict extreme events in the Hénon map. *Chaos* **30** (1), 013113.
LEUTBECHER, M. & PALMER, T.N. 2008 Ensemble forecasting. *J. Comput. Phys.* **227** (7), 3515–3539.
LORENZ, E.N. 1963 Deterministic nonperiodic flow. *J. Atmos. Sci.* **20** (2), 130–141.
LORENZ, E.N. 1965 A study of the predictability of a 28-variable atmospheric model. *Tellus* **17** (3), 321–333.
LOZANO-DURÁN, A., BAE, H.J. & ENCINAR, M.P. 2020 Causality of energy-containing eddies in wall turbulence. *J. Fluid Mech.* **882**, A2.
LUCAS, D. & KERSWELL, R.R. 2015 Recurrent flow analysis in spatiotemporally chaotic 2-dimensional Kolmogorov flow. *Phys. Fluids* **27** (4), 045106.
MACKAY, D.J.C. 2003 *Information Theory, Inference and Learning Algorithms*. Cambridge University Press.
MOHAMAD, M.A. & SAPSIS, T.P. 2018 Sequential sampling strategy for extreme event statistics in nonlinear dynamical systems. *Proc. Natl Acad. Sci. USA* **115** (44), 11138–11143.
PAGE, J., BRENNER, M.P. & KERSWELL, R.R. 2021 Revealing the state space of turbulence using machine learning. *Phys. Rev. Fluids* **6** (3), 034402.
PALMER, T.N. 1993 Extended-range atmospheric prediction and the Lorenz model. *Bull. Am. Meteorol. Soc.* **74** (1), 49–66.
PALMER, T.N. 2000 Predicting uncertainty in forecasts of weather and climate. *Rep. Prog. Phys.* **63** (2), 71.
QI, D. & MAJDA, A.J. 2020 Using machine learning to predict extreme events in complex systems. *Proc. Natl Acad. Sci. USA* **117** (1), 52–59.
RAHMSTORF, S. & COUMOU, D. 2011 Increase of extreme events in a warming world. *Proc. Natl Acad. Sci. USA* **108** (44), 17905–17909.
ROLLAND, J. 2022 Collapse of transitional wall turbulence captured using a rare events algorithm. *J. Fluid Mech.* **931**, A22.
SAPSIS, T.P. 2021 Statistics of extreme events in fluid flows and waves. *Annu. Rev. Fluid Mech.* **53**, 85–111.
STOTT, P. 2016 How climate change affects extreme weather events. *Science* **352** (6293), 1517–1518.
SURI, B., TITHOF, J., GRIGORIEV, R.O. & SCHATZ, M.F. 2017 Forecasting fluid flows using the geometry of turbulence. *Phys. Rev. Lett.* **118** (11), 114501.
TRAVIS, W.R. 2010 Going to extremes: propositions on the social response to severe climate change. *Clim. Change* **98** (1), 1–19.
VELA-MARTÍN, A. & AVILA, M. 2022 Memoryless drop breakup in turbulence. *Sci. Adv.* **8** (50), eabp9561.

VITART, F. & ROBERTSON, A.W. 2018 The sub-seasonal to seasonal prediction project (S2S) and the prediction of extreme events. *NPJ Clim. Atmos. Sci.* **1** (1), 1–7.

WOLF, A., SWIFT, J.B., SWINNEY, H.L. & VASTANO, J.A. 1985 Determining Lyapunov exponents from a time series. *Physica* D **16**, 285–317.

YALNIZ, G., HOF, B. & BUDANUR, N.B. 2021 Coarse graining the state space of a turbulent flow using periodic orbits. *Phys. Rev. Lett.* **126** (24), 244502.

ZIEHMANN, C., SMITH, L.A. & KURTHS, J. 2000 Localized Lyapunov exponents and the prediction of predictability. *Phys. Lett.* A **271** (4), 237–251.